Journal Name

ARTICLE

Controllable vapor phase fabrication of F:Mn_3O_4 thin films functionalized with Ag and TiO_2

Received 00th January 20xx,
Accepted 00th January 20xx

DOI: 10.1039/x0xx00000x

www.rsc.org/

Lorenzo Bigiani,[a] Davide Barreca,*[b] Alberto Gasparotto,[a] Cinzia Sada,[c] Sara Martí-Sanchez,[d] Jordi Arbiol[d,e] and Chiara Maccato*[a]

A facile two-step vapor phase synthetic approach is proposed for the fabrication of Mn_3O_4 thin films chemically modified with fluorine, and eventually functionalized with silver or titania. The adopted strategy exploits the initial chemical vapor deposition (CVD) of Mn_3O_4 on Si(100) substrates starting from a diamine diketonate Mn(II) complex, followed by the controlled radio frequency (RF)-sputtering of silver or titania. Complementary analytical techniques were employed to investigate the crystallinity (X-ray diffraction), chemical composition (X-ray photoelectron spectroscopy, secondary ion mass spectrometry, energy dispersive X-ray spectroscopy), morphology and nano-organization (field emission-scanning electron microscopy, atomic force microscopy, transmission electron microscopy) of both pristine and functionalized manganese oxide thin films. Under the adopted operating conditions, the target Mn(II) complex acted as a single-source precursor for both Mn and F, leading to the formation of phase-pure *haussmannite* Mn_3O_4 films characterized by a uniform in-depth fluorine content. In addition, the obtained results gave evidence of the formation of high purity Ag/F:Mn_3O_4 and TiO_2/F:Mn_3O_4 composites with a close contact between the single constituents. This work outlines an amenable and efficient method for the vapor phase growth of composite Mn_3O_4-based thin films, which stand as favorable candidates for diverse technological applications, from photocatalysis to gas sensing.

Introduction

Mn_3O_4, an earth-abundant and eco-friendly *p*-type semiconductor (E_G = 2.5 eV)[1-3] ENREF 1 with Mn(II) and Mn(III) centers occupying the tetrahedral and octahedral sites of the spinel structure,[3-11] ENREF 1 is an attractive multi-functional oxide in view of numerous technological applications.[12-14] ENREF 8 The latter encompass electrochromic materials,[15] antibacterial systems,[16] supercapacitors,[1, 2, 17] ENREF 4 sensors/biosensors,[13, 18-21] and heterogeneous catalysts for a variety of reactions (oxidation of organic compounds,[16, 22-25] ENREF 2 oxygen evolution reaction,[4, 26-29] ENREF 3 ….). Other reports have concerned the use of Mn_3O_4 as photocatalyst,[20] especially in the purification of contaminated wastewaters,[30, 31] thanks also to its appealing properties and Visible light harvesting,[27] enabling an efficient exploitation of solar radiation.

The functional performances of Mn_3O_4-based systems are directly dependent on their actual composition and morphological organization,[13, 22, 24, 26] ENREF 4 which, in turn, are significantly affected by the adopted processing conditions. Additional degrees of freedom to control the properties of Mn_3O_4 nanosystems involve their chemical modification with suitable elements and functionalization with nanoparticles or thin surface layers. As concerns the former, various studies regarding the introduction of cationic dopants into Mn_3O_4, both for catalytic and gas sensing applications,[4, 13, 20, 25, 32] have been reported so far. Conversely, no examples regarding anionic doping, for instance with fluorine, are available in the literature up to date. Nevertheless, F introduction in metal oxides can: i) increase the electrical conductivity, of importance for sensing end uses; ii) enhance the Lewis acidity of metal centers through the substitution of O by F, boosting thus the resulting catalytic activity; iii) passivate surface defects, suppressing charge carrier recombination phenomena, and enhance the absorption coefficient, favorably affecting photocatalytic properties.[33-36] ENREF 25 ENREF 36 ENREF 11 ENREF 20

Another strategy to tailor Mn_3O_4 properties involves the controlled preparation of nanocomposites with other metals/oxides, which benefit from the synergetic interactions between the system components,[27, 37-39] ENREF 3 resulting in considerable technological advantages.[40] In this regard, among the various possible metals, silver has been identified as a promising candidate and used in the development of Ag/Mn_3O_4 systems for both catalysis[38, 39] and gas sensing.[9] As regards functionalization of Mn_3O_4 with other oxides, the use of titania has been reported in the preparation of TiO_2/Mn_3O_4 composites for the abatement of volatile organic compounds (VOCs),[37, 41] ENREF 3 as well as for the fabrication of advanced lithium ion battery anodes.[42]

In view of the above discussed applications, various synthetic

[a] Department of Chemical Sciences, Padova University and INSTM, Via F. Marzolo 1, 35131 Padova, Italy. E-mail: chiara.maccato@unipd.it
[b] CNR-ICMATE and INSTM, Department of Chemical Sciences, Padova University, Via F. Marzolo 1, 35131 Padova, Italy. E-mail: davide.barreca@unipd.it
[c] Department of Physics and Astronomy, Padova University and INSTM, Via F. Marzolo 8, 35131 Padova, Italy
[d] Catalan Institute of Nanoscience and Nanotechnology (ICN2), CSIC and BIST, Bellaterra, 08193 Barcelona, Catalonia, Spain
[e] ICREA, Pg. Lluís Companys 23, 08010 Barcelona, Catalonia, Spain

† Electronic Supplementary Information (ESI) available: Additional data on XRD, SIMS, XPS, AFM HAADF-STEM and EDXS analyses for the target materials. See DOI: 10.1039/x0xx00000x

strategies have been so far utilized for the preparation of Mn_3O_4-based nanomaterials, including hydrothermal[27] and solution routes,[9, 21-23, 42] as well as thermal decomposition of Mn_2O_3[5] and of Mn salts.[21] Nevertheless, these works have concerned powdered systems, whereas modern nanofabrication frontiers require the preparation of Mn_3O_4 supported nanostructures/thin films with tailored properties,[8] for the ultimate development of various microsystems and devices.[43] To date, Mn_3O_4-based films have been obtained by galvanostatic processes,[8, 15] ENREF 6 chemical solution deposition,[1, 2, 16, 28] ENREF 9 spray pyrolysis,[10, 13, 20, 32] ENREF 7 atomic layer deposition[6, 43, 44] ENREF 3 and chemical vapor deposition (CVD).[7, 11, 45] In spite of these studies, no works have been so far devoted to the preparation of Mn_3O_4 films either doped/modified with F, or functionalized with Ag or TiO_2.

Among the various film preparation routes, CVD techniques have emerged as amenable strategy, offering important benefits in terms of film quality and scale up.[46] In particular, the main CVD advantages are related to the inherent versatility in controlling the structure, morphological organization and chemical composition of the resulting systems,[45] which are significantly affected by the chemical nature of the used molecular precursor.[47]

In our previous studies, we have focused on the investigation of fluorinated $M(hfa)_2$•TMEDA complexes[53] (hfa = 1,1,1,5,5,5-hexafluoro-2,4-pentanedionate; TMEDA = *N*,*N*,*N*′,*N*′-tetramethylethylenediamine) of various elements, including Cu,[48] Co,[49] Fe,[50, 51] as CVD precursors for the preparation of the corresponding oxides.[33-36, 52-54] ENREF 55 In this work, we present an unprecedented fabrication protocol for the development Mn_3O_4 thin films modified with fluorine, eventually functionalized with Ag and TiO_2 (Fig. 1). The target route is based on the CVD of F-containing Mn_3O_4 films starting from $Mn(tfa)_2$•TMEDA (tfa = 1,1,1-trifluoro-2,4-pentanedionate), a compound never used in CVD processes up to date, that simultaneously acts as Mn and F source. In a subsequent step, functionalization of the obtained systems either with Ag or TiO_2 is carried out by radio frequency (RF)-sputtering at low temperatures, so as to prevent undesired chemico-physical modifications of the pristine Mn_3O_4.[55, 56] Particular efforts have been devoted to the achievement of a controlled functionalization, as well as of an intimate contact between Mn_3O_4 and Ag (or TiO_2), of key importance for the exploitation of their synergistic interactions in view of possible functional applications. In this work, insights on growth and properties of the target materials are achieved through a nanoscopic investigation based on the use of complementary techniques, with the aim of unraveling the interplay between preparation conditions and material structure, chemical composition and morphological organization.

Experimental

Synthesis

The precursor $Mn(tfa)_2$•TMEDA, used as manganese molecular source, was synthesized and characterized as recently reported.[57, 58] The deposition of Mn_3O_4 was carried out using a cold-wall horizontal CVD reaction system equipped with a quartz chamber, a resistively heated susceptor and an external precursor reservoir, heated at 65°C. In each experiment, precursor vapors were transported into the reaction chamber by means of a primary O_2 flow [purity = 6.0; flow rate = 100 standard cubic centimeters per minute (sccm)]. To prevent undesired condensation phenomena, gas lines connecting the precursor vessel to the reaction chamber were maintained at 105°C throughout each growth process. An auxiliary O_2 flow (flow rate = 100 sccm) was introduced directly into the reactor. Depositions were carried out at a total pressure of 10.0 mbar for 60 min on Si(100) substrates (MEMC®, Merano, Italy), previously subjected to a cleaning pre-treatment,[52] operating between 300 and 500°C. The use of lower temperatures was discarded, since preliminary experiments resulted in the obtainment of a non-uniform substrate coverage. Subsequently, silver or titania sputtering was carried out on Mn_3O_4 films obtained at 400°C.

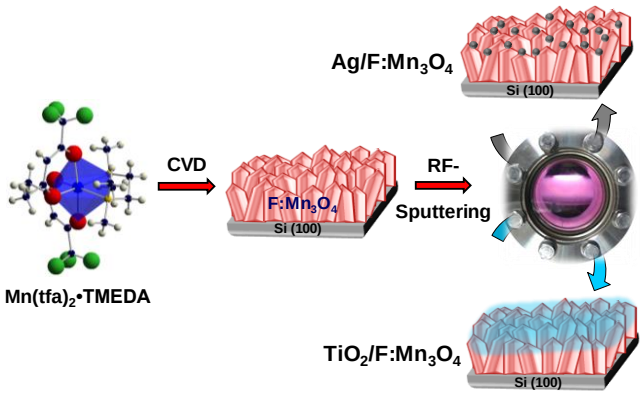

Fig. 1 Sketch of the fabrication route adopted for the synthesis of Ag/F:Mn_3O_4 and TiO_2/F:Mn_3O_4 nanocomposites.

Experiments were performed by using a custom-built two-electrode RF plasmochemical reactor (ν = 13.56 MHz) using Ar (purity = 5.0; flow rate = 10 sccm) as plasma source, and Ag (BALTEC AG, 99.99%) or Ti (Alfa Aesar®, 99.95%) targets for the preparation of Ag/F:Mn_3O_4 and TiO_2/F:Mn_3O_4 systems, respectively. In each experiment, the target was fixed on the RF electrode, whereas Si-supported Mn_3O_4 films were mounted on a second grounded electrode maintained at 60°C. Basing on previously obtained results,[55, 56] experiments were conducted at a total pressure of 0.3 mbar, using a RF-power of 5 (20) W and a deposition time of 45 (180) min for silver (titania) deposition, respectively. The obtained nanocomposites were characterized as such, without any *ex-situ* thermal treatment, to prevent undesired morphological alterations of Mn_3O_4 and its conversion into other Mn oxides.[28, 29, 59]

Characterization

Glancing incidence X-ray diffraction (GIXRD) analyses were performed at an incidence angle of 1.0° using a Bruker D8 Advance diffractometer, equipped with a sealed copper tube (40 kV, 40 mA) attached to a focused Göbel mirror yielding a parallel X-ray beam (CuKα radiation, λ = 0.154 nm).

X-ray photoelectron spectroscopy (XPS) analysis was carried out using a Perkin-Elmer Φ5600ci spectrometer, using a standard AlKα X-ray source (1486.6 eV). The binding energy (BE) scale (uncertainty = ±0.2 eV) was referenced to to the C1s line of adventitious carbon at 284.8 eV.[60] The analysis involved Shirley-type background subtraction,[61] and, whenever necessary, fitting by a non-linear least-square procedure, adopting Gaussian-Lorentzian peak shapes. Atomic percentages (at. %) were calculated using Φ V5.4A sensitivity factors. The Ag(0) and Ag(I) oxidation states were discriminated using silver Auger α_1 and α_2 parameters, calculated as previously reported.[55, 60, 62]

Secondary ion mass spectrometry (SIMS) measurements were carried out by means of a Cameca IMS 4f instrument, using a Cs^+ primary ion beam (14.5 keV, 20 nA) and by negative secondary ion

detection. Signals were collected by rastering over a 150×150 μm² area, detecting secondary ions from a sub-region close to 8×8 μm² in order to prevent undesired crater effects. Charge compensation was performed by using an electron gun. Analyses were carried out in high mass resolution configuration, to avoid mass interference artifacts, and in beam blanking mode, to achieve an improved in-depth resolution. The sputtering time was converted into depth values using the deposit thickness data measured by cross-sectional field emission-scanning electron microscopy (FE-SEM) analysis.

FE-SEM images were collected by using a Zeiss SUPRA 40VP instrument equipped with an Oxford INCA x-sight X-ray detector for energy dispersive X-ray spectroscopy (EDXS) investigation. Plane-view and cross-sectional micrographs were recorded using primary beam acceleration voltages between 10.0 and 20.0 kV, collecting secondary and back-scattered electron signals (SE and BSE, respectively). The average nanodeposit thickness and aggregate dimensions were evaluated using the ImageJ® software (http://imagej.nih.gov/ij/, accessed September 2017). The maximum uncertainty on the reported EDXS % values is ±0.2%.

Atomic force microscopy (AFM) analyses were recorded in tapping mode using an NT-MDT SPM Solver P47H-PRO instrument equipped with an anti-noise table. Root Mean Square (RMS) roughness values were evaluated through the NT-MDT software after background subtraction.

High resolution-transmission electron microscopy (HR-TEM) in combination with scanning TEM in high angle annular dark field mode (HAADF-STEM) characterization was performed with a FEI Tecnai F20 TEM operated at 200 kV. For structural analyses, power spectra (FFT) were obtained on selected areas of HRTEM micrographs by using the Gatan Digital Micrograph software and indexing the reciprocal space patterns by direct comparison with structural atomic models created by Carine Crystallography software.[63] Compositional analysis was obtained by combining HAADF-STEM with EDXS. The films were prepared for cross-sectional (S)TEM characterization by diamond wire saw cutting, mechanical thinning with diamond lapping films in a conventional polisher, and ion milling in a Gatan precision ion polishing system (PIPS).

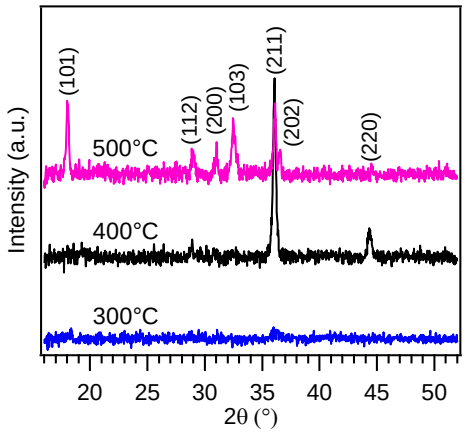

Fig. 2 Representative GIXRD patterns of manganese oxide thin films deposited onto Si(100) at different growth temperatures.

Results and discussion

Mn_3O_4 thin films

The first part of the present study was dedicated to a preliminary screening of the interplay between the growth temperature (*T*) and chemico-physical properties of the resulting Mn_3O_4 films. In this regard, a valuable insight into the system microstructure was obtained by XRD analyses (Fig. 2). As a general observation, the sample grown at 300°C showed a poor crystallinity, whereas well developed diffraction signals could be obtained for *T* = 400°C. In this case, all the observed peaks could be assigned to reflections of tetragonal α-Mn_3O_4 (*haussmannite*; space group: $I4_1/amd$; lattice parameters *a* = 5.75 Å, *c* = 9.42 Å), the most stable Mn_3O_4 phase under ordinary conditions.[3, 5, 17, 22, 64] A comparison of the relative intensities with the corresponding ones of the reference *haussmannite* powder spectrum suggested the preferential exposure of (211) planes and/or the occurrence of an anisotropic crystallite growth,[65] in line with the corresponding texture coefficient value (TC_{211} = 1.1, § S-2.1†). An increase of *T* to 500°C produced the appearance of additional peaks, and the enhanced thermal energy supply resulted in a (101) orientation (TC_{101} = 2.2, § S-2.1†), thereby evidencing the influence of deposition temperature on the material structural organization. Correspondingly, calculations of the mean crystallite dimensions by the Scherrer equation highlighted an increase from 25 to 35 nm upon going from 400 to 500°C, suggesting a parallel increase of the overall system crystallinity.

The determined dislocation density (δ) and microstrain (ε) values (§ S-2.1†) yielded 9.0×10^{14} lines×m² and 0.21 for a growth temperature of 400°C, whereas the corresponding δ and ε at *T* = 500°C were estimated to be 5.2×10^{14} and 0.16. The obtained values were found to be in agreement with those pertaining to Mn_3O_4 thin films obtained by spraying.[10] Taken together, these data suggest that, beside improving the crystalline quality, a growth temperature enhancement results in a decrease of the number of defects in the target thin films.

The surface chemical composition of the target Mn_3O_4 systems was investigated by XPS. Fig. 3(a) displays a representative wide-scan spectrum, which was dominated by Mn and O signals,

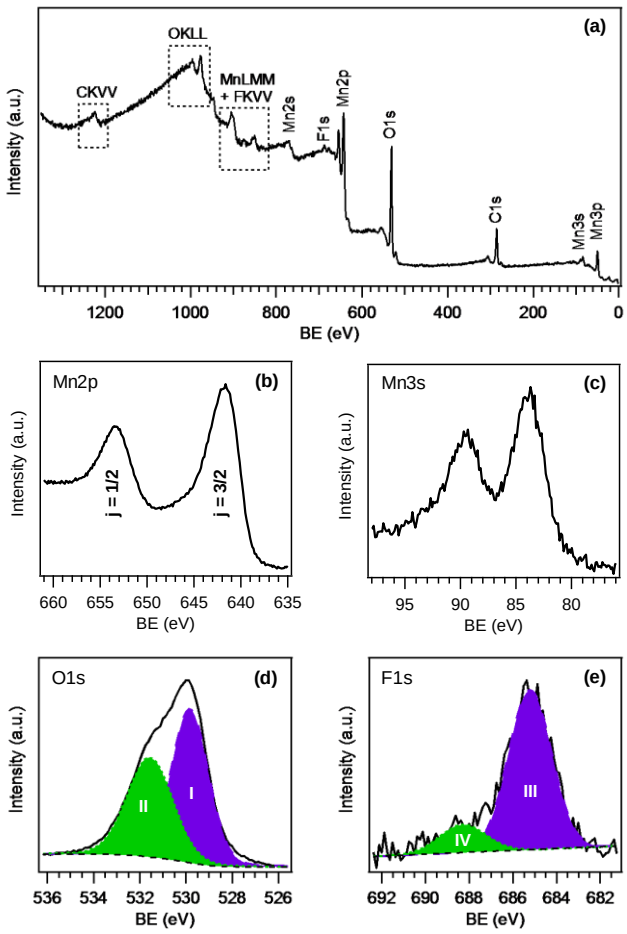

Fig. 3 (a) Surface wide-scan XPS spectrum of a manganese oxide specimen grown at 400°C. The detailed Mn2p (b), Mn3s (c), O1s (d) and F1s (e) photopeaks are also displayed.

along with minor C and F peaks. The typical carbon concentration was ≈10%, and its presence was mainly related to external contamination (see SIMS data below). For all the investigated systems, the Mn2p peak spectral shape and position [Fig. 3(b); BE($Mn2p_{3/2}$) = 641.9 eV; spin-orbit splitting (SOS) = 11.6 eV] were in good agreement with previously reported data for Mn_3O_4.[8, 14, 18, 19, 21, 24-29] The two spin-orbit components are relatively broad due to the concurrent contribution of Mn(II) and Mn(III) oxidation states and the occurrence of multiplet splitting phenomena, arising from the existence of unpaired electrons in Mn valence level.[60] These issues prevent the obtainment of a reliable Mn2p fitting with the correct relative intensities of manganese(II) and manganese (III) species, whose mutual contents are directly influenced by the adopted fitting procedure, yielding thus controversial data.[14, 18, 25, 26, 28, 59, 66] Due to the difficulties in determining manganese oxidation state by the analysis of the sole Mn2p signal, attention was also devoted to the analysis of the BE spacing of the two Mn3s components [Fig. 3(c)], arising from multiplet splitting.[60] The obtained value [ΔBE(3s) = 5.4 eV] confirmed the formation of the sole Mn_3O_4, free from other Mn oxides,[15, 17, 43, 58, 62] a conclusion further corroborated by the evaluation of the energy difference between the $Mn2p_{3/2}$ maximum and the lowest O1s BE component (112.0 eV).[6, 15, 27] ENREF 3 The O1s signal [Fig. 3(d)] could be deconvoluted by means of a principal component at BE = 529.9 eV (**I**), referred to lattice oxygen, and a second one at BE = 531.5 eV (**II**), attributed to the presence of hydroxyl or carbonate species due to air exposure.[27, 33, 38, 42, 57, 62, 66] For this reason, the O/Mn atomic ratio (1.9) turned out to be higher than the stoichiometric ones expected for Mn_3O_4. The F1s photopeak in Fig. 3(e) (F/Mn atomic ratio = 0.48) was fitted by two components at BE = 685.1 eV (**III**) and 688.3 eV (**IV**), which could be attributed to the incorporation of fluorine in the oxide network and to CF_x precursor residuals, respectively.[33-36, 57, 62] These results suggested a successful F introduction in Mn_3O_4 films, as a direct consequence of the use of a fluorinated molecular precursor for the CVD process. Regarding Mn_3O_4 system, this is an unprecedented result which could be of great importance to tailor the system functional properties for different applications, as already mentioned. The successful occurrence of F introduction was confirmed by EDXS [typical values: 48.2% (Mn), 31.6 (O) and 19.6 (F) and by in-depth SIMS analyses (Fig. S1†), which highlighted an even fluorine dispersion throughout the deposit thickness. The samples presented a net interface with the Si(100) substrate, and the parallel trends of O, Mn and F indicated an homogeneous system composition. As a general rule, the average C content in the analysed nanodeposits was estimated to be as low as tenths of ppm, indicating a clean conversion of $Mn(hfa)_2$•TMEDA into Mn_3O_4.

FE-SEM and AFM measurements were carried out on selected systems to investigate the morphology and nano-organization occurring as a function of the growth temperature. As can be noticed in Figs. 4(a) and 4(c), the films were characterized by a uniform distribution of highly interconnected nanoaggregates, whose assembly resulted in the formation of relatively compact deposits. The morphology observed at 400°C was very similar to that reported for Mn_3O_4 films obtained by chemical bath deposition.[3] The mean nanoaggregate sizes underwent an increase from (48 ± 12) nm to (84 ± 18) nm upon increasing the growth temperature from 400 to 500°C, similarly to the crystallite size values obtained by XRD analyses (see above). A comparison of the grain dimensions with the above values suggested that the observed nanoaggregates were composed by the agglomeration of various crystallites.[59] Cross-sectional micrographs in Figs. 4(b) and 4(d) highlighted the formation of relatively dense deposits, which were well adherent to the Si(100) substrates and

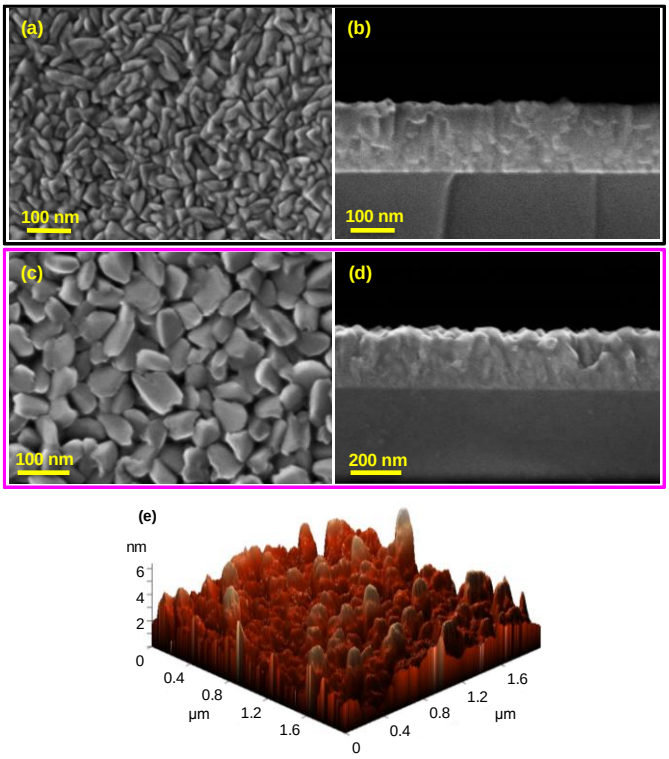

Fig. 4 Plane-view and cross-sectional FE-SEM image for manganese oxide thin films deposited at 400°C (a,b) and 500°C (c,d). Representative AFM micrograph for the sample grown at 400°C.

displayed a thickness increase with temperature [from (170±6) to (250±15) nm upon going from 400 to 500°C; average growth rate = 3.5 nm×min^{-1}] These results suggested the occurrence of a three-dimensional (3D) growth mechanism and of a kinetically controlled growth regime, with surface reactions being the rate-determining process steps.[53, 54] AFM analyses [Fig. 4(e)] confirmed the presence of homogeneously distributed rounded agglomerates, yielding RMS roughness values close to 1.0 nm irrespective of the adopted deposition temperature. Similar roughness values have been reported for Mn oxide thin films fabricated by ALD.[44] Images taken on different sample areas enabled to ascertain surface homogeneity and the absence of any appreciable delamination effect and/or cracks/pinholes.

Ag/F:Mn_3O_4 and TiO_2/F:Mn_3O_4 nanocomposites

The proof-of-concept functionalization of Mn_3O_4 with Ag and TiO_2 by means of RF-sputtering was conducted on films grown at 400°C. Preliminary surface compositional analyses were carried out by XPS (Fig. S2†). A detailed inspection of the corresponding Mn2p signals and a comparison with data presented in Fig. 3 did not reveal any significant variation of the peak positions and shapes, indicating that the pristine F:Mn_3O_4 systems maintained their chemical identity. Beside the expected Mn, O and F peaks, wide scan spectra (Fig. S2a†) highlighted the presence of silver or titanium signals after Ag or Ti RF-sputtering, respectively. As concerns silver [Fig. 5(a)], the Ag3d$_{5/2}$ photopeak was centered at a BE of 368.5 eV. The very close BE values reported for Ag(0) and Ag(I) species prevent from their unambiguous discrimination by Ag3d peak deconvolution.[38, 39, 55] ENREF 55 To obtain a finger print of the actual silver oxidation states, the evaluation of silver Auger parameters (see the Experimental Section) was performed, yielding α_1 and α_2 values of 719.5 and 725.5 eV, respectively. A comparison of these values with reference literature ones[55, 62, 67] ENREF 55

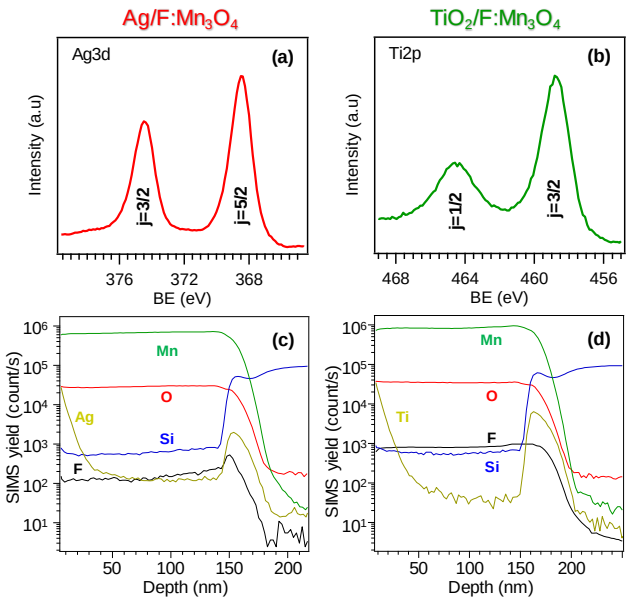

Fig. 5 Surface Ag3d (a) and Ti2p (b) XPS peaks for Ag/F:Mn_3O_4 and TiO_2/F:Mn_3O_4 samples, respectively. SIMS depth profiles for (c) Ag/F:Mn_3O_4 and (d) TiO_2/F:Mn_3O_4 specimens.

suggested a coexistence of the two Ag oxidation states in comparable amounts. The partial oxidation of silver nanoparticles (see also TEM results below) dispersed on oxide matrices by RF-sputtering has already been observed and ascribed to their contact with both the target oxide and the outer atmosphere.[55, 67] In a different way, the Ti2p peak features [Fig. 5(b); BE(Ti2p$_{3/2}$)= 458.8 eV; SOS = 5.7 eV] agreed to a good extent with the presence of Ti(IV) in a titania network.[42, 56, 62] Under the presently adopted conditions, the Ag/Mn and Ti/Mn surface atomic ratios were evaluated to be 1.9 and 0.6, respectively. As shown in Fig. S2(a)†, the presence of manganese was always observed on the sample surface, suggesting either a certain dispersion of Ag and TiO_2 on the Mn_3O_4 deposits, or the formation of very thin overlayers.

SIMS depth profiles in Fig. 5(c) and Fig. 5(b) show that, regarding Mn, O and F, the ionic yield trends were perfectly in line with those already discussed for F:Mn_3O_4 (see above and Fig. S1†). The high sensitivity of the SIMS technique enabled to observe a surface enrichment of Ag and Ti in the deposit region corresponding to the first 50 nm. The corresponding ionic yields *vs*. depth trends could be described by erfchian profiles,[56, 68] ENREF 56 with progressively decreasing intensities at higher depths. This phenomenon could be traced back to the inherent infiltration power of the RF-sputtering technique, further enhanced by plasma bombardment.[56, 67] ENREF 56 Overall, the intimate Ag/F:Mn_3O_4 and TiO_2/F:Mn_3O_4 contact candidates the target materials as intriguing platforms for eventual photocatalytic and gas sensing applications. These results highlighted that the proposed preparation route enabled an effective functionalization of Mn_3O_4 with Ag and TiO_2, the latter being mainly confined in the outermost system layers. Upon RF-sputtering, the surface morphology did not apparently undergo remarkable variations, as suggested by AFM analysis (Fig. S3†), that showed a uniform arrangement of dense nanograins as in the pristine Mn_3O_4 film. The results obtained by FE-SEM and EDXS analysis are reported

in Fig. 6. As concerns Ag/Mn_3O_4 composites, plane-view micrographs, in particular recorded by BSE imaging [Fig. 6(a)], clearly evidenced a uniform dispersion of almost spherical Ag-containing particles, with a mean diameter of (13±3) nm onto Mn_3O_4. The appearance of the cross-sectional structure confirmed no significant thickness variation with respect to the pristine film [compare Fig. 4(b) with Fig. 6(b)]. Cross-sectional EDXS line scans [Fig. 6(e)], in accordance with the above discussed SIMS results, highlighted the even formation of Mn_3O_4 from the outermost region to the interface, as indicated by the intensities of O and Mn X-ray signals that closely followed the same trend throughout the sampled depth. F intensity remained almost constant and a similar trend could also be observed in the case of Ag, which, however, showed an accumulation in the near-surface regions. EDXS spectra recorded on different specimen regions confirmed a homogenous composition, with the following values: 47.3% (Mn), 31.5 (O), 18.9 (F), 2.3 (Ag). In the case of $TiO_2/F:Mn_3O_4$ systems [Fig. 6(c) and Fig. 6(d)], a slightly more rounded surface morphology with respect to the initial $F:Mn_3O_4$ deposit [see Fig. 4(c)] was observed, but the analyses were more elusive, since no clear sign of TiO_2 presence could be obtained.

In order to gain a deeper insight into the nano-organization of the developed composite systems, TEM analyses were undertaken. The low-magnification HAADF-STEM micrographs obtained on $Ag/F:Mn_3O_4$/[110]Si and $TiO_2/F:Mn_3O_4$/[110]Si (Fig. S4†) revealed an average thickness close to 160 nm, in good agreement with the values measured by cross-sectional FE-SEM analyses. EDXS spectra obtained on different regions revealed the presence of Ag nanoparticles in the top surface of the Mn_3O_4 layer in the case of $Ag/F:Mn_3O_4$ sample, whereas TiO_2 was detected on the top surface of $TiO_2/F:Mn_3O_4$. Figs. 7(a)-(d) report representative results regarding an Ag/Mn_3O_4 sample. Fig. 7(a) displays HR-TEM details of the $F:Mn_3O_4$ film. The corresponding power spectrum in Fig. 7(b) shows that the film is polycrystalline. One of the crystals has been identified in the power spectrum, corresponding to a domain that shows {220} and {200} planes in the [001] zone axis. In Fig.7(c), one of the Ag nanoparticles decorating the top surface of $F:Mn_3O_4$ film is imaged. The observed Ag nanoparticles presented a broad size distribution.

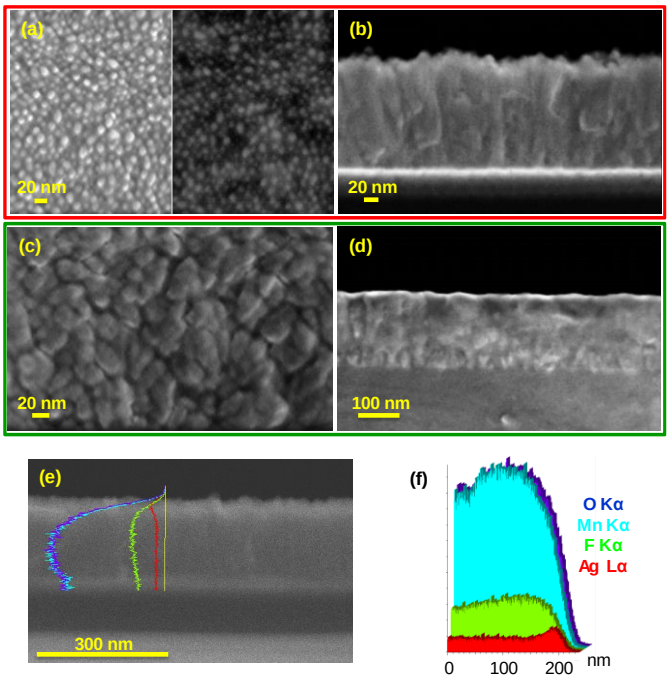

Fig. 6 Plane-view and cross-sectional FE-SEM micrographs for $Ag/F:Mn_3O_4$ (a,b) and $TiO_2/F:Mn_3O_4$ (c,d) samples. In the former case, images were collected by recording SE (left) and BSE (right) electron signals. (e,f) Cross-sectional EDXS line-scans for an $Ag/F:Mn_3O_4$ sample.

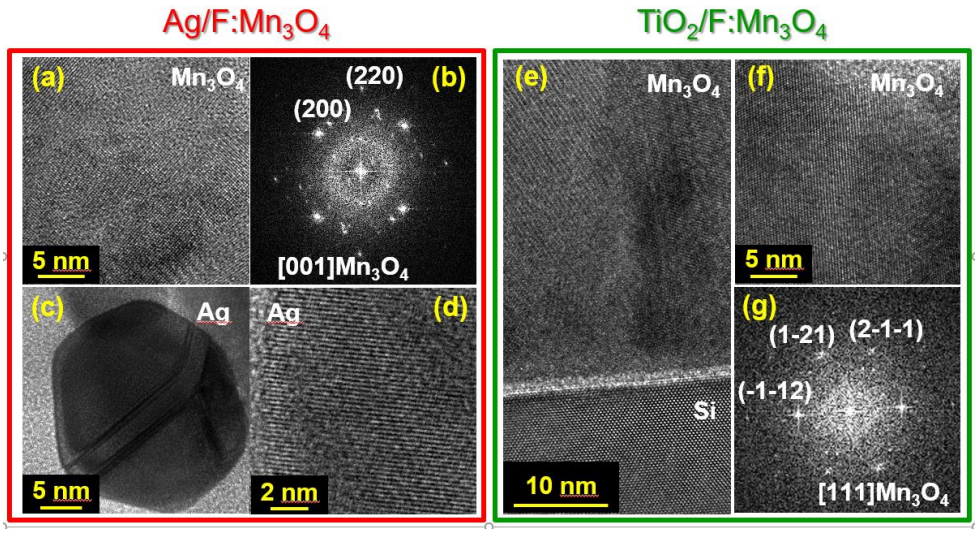

Fig. 7 TEM characterization of $Ag/F:Mn_3O_4$ (a-d) and $TiO_2/F:Mn_3O_4$ (e-g) specimens. (a) HR-TEM micrograph recorded on the Mn_3O_4 film and (b) corresponding indexed power spectrum, revealing the layer polycrystalline nature. (c) Low magnification micrograph on a silver nanoparticle showing some twin defects (dark lines crossing the middle region). (d) Details of the nanoparticle structure. (e) HR-TEM micrograph showing the interface between Mn_3O_4 polycrystalline layer and the [110] oriented silicon substrate. A native oxide layer can be observed at the interface. (f) HR-TEM micrograph obtained on a region of the Mn_3O_4 layer and (g) corresponding indexed power spectrum.

Larger nanoaggregates were found to be defected, containing frequently a set of twins as observed in Fig. 7(c). The presence of twin defects in noble metal nanoparticles is a common effect occurring to minimize the overall surface energy and let the nanoparticles expose a higher number of {111} facets.[69] Further details on the Ag nanoparticle crystallinity are shown in Fig. 7(d).

Figs. 7(e)-(g) report representative results regarding a TiO_2/F:Mn_3O_4 specimen. Even in this case, the results evidenced a [001]-oriented Si Substrate with a polycrystalline Mn_3O_4 film crystallizing in the tetragonal $I4_1/amd$ system. The presence of a 2 nm amorphous native SiO_2 layer on top of the substrate prevented any epitaxial growth under the adopted conditions (see also Fig. 7(e)). The crystal in Fig. 7(f) and indexed in the power spectrum of Fig. 7(g) was found to be oriented along the [111] zone axis. However, no crystalline planes corresponding to TiO_2 could be clearly observed on top of the Mn_3O_4 films. Taken together, these results, along with XRD, XPS and SIMS data, suggest the formation of an ultra-thin (≈1-2 nm) amorphous TiO_2 layer on the underlying Mn_3O_4. The formation of an amorphous and ultra-thin TiO_2 film under analogous RF-sputtering conditions has indeed been observed even for iron–titanium oxide nanocomposites fabricated by a similar route.[56]

Conclusions

This work has been focused on the controlled fabrication of F:Mn_3O_4 thin films functionalized with Ag or TiO_2 by means of a vapor-phase route. The target process consisted in the initial CVD of Mn_3O_4 thin films under O_2 atmospheres starting from $Mn(tfa)_2$•TMEDA. Variations of the growth temperature in CVD processes enabled the preparation of pure Mn_3O_4 thin films comprising the sole *haussmannite* phase, characterized by tailored structural and morphological characteristics. Under the adopted conditions, the target $Mn(tfa)_2$•TMEDA compound acted as a single-source precursor for manganese and fluorine, enabling the synthesis of F-containing Mn_3O_4 films, with fluorine uniformly distributed throughout the nanodeposits depth. Subsequently, a proof-of-concept functionalization of the target systems with Ag and TiO_2 by means of RF-sputtering has been successfully demonstrated. Thanks to the mild conditions and the inherent infiltration power characterizing the used sputtering processes, Ag/F:Mn_3O_4 and TiO_2/F:Mn_3O_4 composites with a close contact between the constituents could be clearly obtained. Whereas in the former case an even dispersion of partially oxidized silver particles could be obtained, in the latter the formation of a thin and amorphous titania overlayer covering the underlying Mn_3O_4 nanodeposit took place. As a result, Mn_3O_4-based composites modified by fluorine incorporation and the introduction of silver and titania could be readily obtained. To the best of our knowledge, a similar result has never been reported in the literature up to date.

The used preparation route is flexible, solvent-free and amenable to scale-up, features that render it a promising avenue in view of eventual technological applications. Basing on the presented results, attractive perspectives for future developments will concern a more detailed investigation aimed at elucidating the molecule-to-material conversion mechanism in the CVD processes, to shed light on fluorine incorporation into Mn_3O_4 and pave the way to a detailed control of F content. In addition, both the dispersion of silver particles and the coverage with TiO_2 of Mn_3O_4 systems, resulting in the formation of heterojunctions, hold an attractive promise for the development of gas sensors,[70] as well as photocatalytic hydrogen generation and/or wastewater purification. Further studies are already in progress along these research lines.

Conflicts of interest

The authors declare no conflicts of interest.

Acknowledgements

This work was financially supported by Padova University DOR 2016–2017 and P-DiSC #03BIRD2016-UNIPD projects. Funding from "Programa Internacional de Becas "la Caixa"-Severo Ochoa" and from Generalitat de Catalunya 2017 SGR 327 and the Spanish MINECO ENE2017-85087-C3-3-R is also acknowledged. ICN2 acknowledges support from the Severo Ochoa Program (MINECO, Grant SEV-2013-0295) and is funded by the CERCA Programme/Generalitat de Catalunya. Part of the present work has been performed in the framework of Universitat Autònoma de Barcelona Materials Science PhD program. Thanks are also due to Dr. Giorgio Carraro (Department of Chemical Sciences, Padova University, Italy) for precious help and assistance.

References

1 D. P. Dubal, D. S. Dhawale, R. R. Salunkhe, S. M. Pawar and C. D. Lokhande, *Appl. Surf. Sci.*, 2010, **256**, 4411-4416.
2 D. P. Dubal, D. S. Dhawale, R. R. Salunkhe, V. J. Fulari and C. D. Lokhande, *J. Alloys Compd.*, 2010, **497**, 166-170.
3 H. Y. Xu, S. Le Xu, X. D. Li, H. Wang and H. Yan, *Appl. Surf. Sci.*, 2006, **252**, 4091-4096.
4 V. Maruthapandian, T. Pandiarajan, V. Saraswathy and S. Muralidharan, *RSC Adv.*, 2016, **6**, 48995-49002.
5 J. Darul, C. Lathe and P. Piszora, *J. Phys. Chem. C*, 2013, **117**, 23487-23494.
6 F. Mattelaer, T. Bosserez, J. Ronge, J. A. Martens, J. Dendooven and C. Detavernier, *RSC Adv.*, 2016, **6**, 98337-98343.
7 O. Y. Gorbenko, I. E. Graboy, V. A. Amelichev, A. A. Bosak, A. R. Kaul, B. Guttler, V. L. Svetchnikov and H. W. Zandbergen, *Solid State Commun.*, 2002, **124**, 15-20.
8 A. Ramírez, P. Hillebrand, D. Stellmach, M. M. May, P. Bogdanoff and S. Fiechter, *J. Phys. Chem. C*, 2014, **118**, 14073-14081.
9 H. Rahaman, S. Kundu and S. K. Ghosh, *ChemistrySelect*, 2017, **2**, 6991-6999.
10 T. Larbi, B. Ouni, A. Boukhachem, K. Boubaker and M. Amlouk, *Mater. Res. Bull.*, 2014, **60**, 457-466.
11 Z.-Y. Tian, P. Mountapmbeme Kouotou, N. Bahlawane and P. H. Tchoua Ngamou, *J. Phys. Chem. C*, 2013, **117**, 6218-6224.
12 Z. Chen, Z. Jiao, D. Pan, Z. Li, M. Wu, C.-H. Shek, C. M. L. Wu and J. K. L. Lai, *Chem. Rev.*, 2012, **112**, 3833-3855.
13 L. Ben Said, A. Inoubli, B. Bouricha and M. Amlouk, *Spectrochim. Acta, Part A*, 2017, **171**, 487-498.
14 Y. Hu, L. Li, L. C. Zhang and Y. Lv, *Sens. Actuators, B*, 2017, **239**, 1177-1184.
15 M. Chigane and M. Ishikawa, *J. Electrochem. Soc.*, 2000, **147**, 2246-2251.
16 M. R. Belkhedkar and A. U. Ubale, *Jo. Mol. Struct.*, 2014, **1068**, 94-100.
17 K. B. Wang, X. Y. Ma, Z. Y. Zhang, M. B. Zheng, Z. R. Geng and Z. L. Wang, *Chem. Eur. J.*, 2013, **19**, 7084-7089.
18 C. W. Na, S.-Y. Park, J.-H. Chung and J.-H. Lee, *ACS Appl. Mater. Interfaces*, 2012, **4**, 6565-6572.
19 S. L. Yang, L. X. Liu, G. F. Wang, G. Li, D. H. Deng and L. B. Qu, *J. Electroanal. Chem.*, 2015, **755**, 15-21.
20 M. A. Amara, T. Larbi, A. Labidi, M. Karyaoui, B. Ouni and M. Amlouk, *Mater. Res. Bull.*, 2016, **75**, 217-223.
21 J. K. Sharma, P. Srivastava, S. Ameen, M. S. Akhtar, G. Singh and S. Yadava, *J. Colloid Interface Sci.*, 2016, **472**, 220-228.
22 C. Chen, G. J. Ding, D. Zhang, Z. Jiao, M. H. Wu, C. H. Shek, C. M. L. Wu, J. K. L. Lai and Z. W. Chen, *Nanoscale*, 2012, **4**, 2590-2596.
23 H. Dong, E. K. Koh and S.-Y. Lee, *J. Nanosci. Nanotechnol.*, 2009, **9**, 6511-6517.
24 Z.-Y. Fei, B. Sun, L. Zhao, W.-J. Ji and C.-T. Au, *Chem. Eur. J.*,

2013, **19**, 6480-6487.
25 C. Anil and G. Madras, *J. Mol. Catal. A: Chem.*, 2016, **424**, 106-114.
26 J. Liu, L. H. Jiang, T. R. Zhang, J. T. Jin, L. Z. Yuan and G. Q. Sun, *Electrochim. Acta*, 2016, **205**, 38-44.
27 N. Li, Y. Tian, J. Zhao, J. Zhang, J. Zhang, W. Zuo and Y. Ding, *Appl. Catal., B*, 2017, **214**, 126-136.
28 H. S. Jeon, S. J. Ahn, M. S. Jee, S. S. Yoon, Y. J. Hwang and B. K. Min, *J. Electrochem. Soc.*, 2016, **163**, F3113-F3118.
29 G. Y. Liu, J. Hall, N. Nasiri, T. Gengenbach, L. Spiccia, M. H. Cheah and A. Tricoli, *ChemSusChem*, 2015, **8**, 4162-4171.
30 K. A. M. Ahmed, H. Peng, K. Wu and K. Huang, *Chem. Eng. J.*, 2011, **172**, 531-539.
31 K. Govindan, H. T. Chandran, M. Raja, S. U. Maheswari and M. Rangarajan, *J. Photochem. Photobiol., A*, 2017, **341**, 146-156.
32 T. Larbi, M. H. Lakhdar, A. Amara, B. Ouni, A. Boukhachem, A. Mater and M. Amlouk, *J. Alloys Compd.*, 2015, **626**, 93-101.
33 G. Carraro, D. Barreca, D. Bekermann, T. Montini, A. Gasparotto, V. Gombac, C. Maccato and P. Fornasiero, *J. Nanosci. Nanotechnol.*, 2013, **13**, 4962-4968.
34 G. Carraro, A. Gasparotto, C. Maccato, E. Bontempi, O. I. Lebedev, S. Turner, C. Sada, L. E. Depero, G. Van Tendeloo and D. Barreca, *RSC Adv.*, 2013, **3**, 23762-23768.
35 A. Gasparotto, D. Barreca, D. Bekermann, A. Devi, R. A. Fischer, P. Fornasiero, V. Gombac, O. I. Lebedev, C. Maccato, T. Montini, G. Van Tendeloo and E. Tondello, *J. Am. Chem. Soc.*, 2011, **133**, 19362-19365.
36 D. Barreca, D. Bekermann, E. Comini, A. Devi, R. A. Fischer, A. Gasparotto, M. Gavagnin, C. Maccato, C. Sada, G. Sberveglieri and E. Tondello, *Sens. Actuators, B*, 2011, **160**, 79-86.
37 Y. Ma, Y. Li, M. Mao, J. Hou, M. Zeng and X. Zhao, *J. Mater. Chem. A*, 2015, **3**, 5509-5516.
38 J. J. Liu, J. Z. Liu, W. W. Song, F. Wang and Y. Song, *J. Mater. Chem. A*, 2014, **2**, 17477-17488.
39 S. S. Acharyya, S. Ghosh, S. K. Sharma and R. Bal, *New J. Chem.*, 2016, **40**, 3812-3820.
40 C. Ray and T. Pal, *J. Mater. Chem. A*, 2017, **5**, 9465-9487.
41 I. Aouadi, J. M. Tatibouët and L. Bergaoui, *Plasma Chem. Plasma Process.*, 2016, **36**, 1485-1499.
42 N. N. Wang, J. Yue, L. Chen, Y. T. Qian and J. Yang, *ACS Appl. Mater. Interfaces*, 2015, **7**, 10348-10355.
43 H. Jin, D. Hagen and M. Karppinen, *Dalton Trans.*, 2016, **45**, 18737-18741.
44 O. Nilsen, H. Fjellvåg and A. Kjekshus, *Thin Solid Films*, 2003, **444**, 44-51.
45 Z. Lipani, M. R. Catalano, P. Rossi, P. Paoli and G. Malandrino, *Chem. Vap. Deposition*, 2013, **19**, 22-28.
46 A. Devi, *Coord. Chem. Rev.*, 2013, **257**, 3332-3384.
47 C. E. Knapp and C. J. Carmalt, *Chem. Soc. Rev.*, 2016, **45**, 1036-1064.
48 G. Bandoli, D. Barreca, A. Gasparotto, R. Seraglia, E. Tondello, A. Devi, R. A. Fischer, M. Winter, E. Fois, A. Gamba and G. Tabacchi, *Phys. Chem. Chem. Phys.*, 2009, **11**, 5998-6007.
49 G. Bandoli, D. Barreca, A. Gasparotto, C. Maccato, R. Seraglia, E. Tondello, A. Devi, R. A. Fischer and M. Winter, *Inorg. Chem.*, 2009, **48**, 82-89.
50 D. Barreca, G. Carraro, A. Devi, E. Fois, A. Gasparotto, R. Seraglia, C. Maccato, C. Sada, G. Tabacchi, E. Tondello, A. Venzo and M. Winter, *Dalton Trans.*, 2012, **41**, 149-155.
51 D. Barreca, G. Carraro, A. Gasparotto, C. Maccato, R. Seraglia and G. Tabacchi, *Inorg. Chim. Acta*, 2012, **380**, 161-166.
52 D. Barreca, A. Gasparotto, C. Maccato, E. Tondello, O. I. Lebedev and G. Van Tendeloo, *Cryst. Growth Des.*, 2009, **9**, 2470-2480.
53 D. Barreca, A. Gasparotto, O. I. Lebedev, C. Maccato, A. Pozza, E. Tondello, S. Turner and G. Van Tendeloo, *CrystEngComm*, 2010, **12**, 2185-2197.
54 G. Carraro, C. Maccato, E. Bontempi, A. Gasparotto, O. I. Lebedev, S. Turner, L. E. Depero, G. Van Tendeloo and D. Barreca, *Eur. J. Inorg. Chem.*, 2013, **2013**, 5454-5461.
55 L. Armelao, D. Barreca, G. Bottaro, A. Gasparotto, C. Maccato, E. Tondello, O. I. Lebedev, S. Turner, G. Van Tendeloo, C. Sada and U. Lavrenčič Štangar, *ChemPhysChem*, 2009, **10**, 3249-3259.
56 D. Barreca, G. Carraro, A. Gasparotto, C. Maccato, M. E. A. Warwick, E. Toniato, V. Gombac, C. Sada, S. Turner, G. Van Tendeloo and P. Fornasiero, *Adv. Mater. Interfaces*, 2016, **3**, 1600348.
57 D. Barreca, G. Carraro, E. Fois, A. Gasparotto, F. Gri, R. Seraglia, M. Wilken, A. Venzo, A. Devi, G. Tabacchi and C. Maccato, *J. Phys. Chem. C*, 2018, **122**, 1367-1375.
58 C. Maccato, L. Bigiani, G. Carraro, A. Gasparotto, R. Seraglia, J. Kim, A. Devi, G. Tabacchi, E. Fois, G. Pace, V. Di Noto and D. Barreca, *Chem. Eur. J.*, 2017, **23**, 17954-17963.
59 A. Moses Ezhil Raj, S. G. Victoria, V. B. Jothy, C. Ravidhas, J. Wollschläger, M. Suendorf, M. Neumann, M. Jayachandran and C. Sanjeeviraja, *Appl. Surf. Sci.*, 2010, **256**, 2920-2926.
60 D. Briggs and M. P. Seah, *Practical Surface Analysis: Auger and X-ray Photoelectron Spectroscopy*, John Wiley & Sons: New York, 2nd ed., 1990.
61 D. A. Shirley, *Phys. Rev. B*, 1972, **5**, 4709-4714.
62 J. F. Moulder, W. F. Stickle, P. E. Sobol and K. D. Bomben, *Handbook of X-ray Photoelectron Spectroscopy*, Perkin Elmer Corperation, Eden Prairie, MN, USA, 1992.
63 J. Arbiol, A. Cirera, F. Peiró, A. Cornet, J. R. Morante, J. J. Delgado and J. J. Calvino, *Appl. Phys. Lett.*, 2002, **80**, 329-331.
64 Pattern N° 024-0734, JCPDS (2000).
65 E. J. Mittemeijer and P. Scardi, *Diffraction Analysis of the Microstructure of Materials*, Berlin-Heidelberg: Springer Verlag, 2004.
66 E. S. Ilton, J. E. Post, P. J. Heaney, F. T. Ling and S. N. Kerisit, *Appl. Surf. Sci.*, 2016, **366**, 475-485.
67 Q. Simon, D. Barreca, D. Bekermann, A. Gasparotto, C. Maccato, E. Comini, V. Gombac, P. Fornasiero, O. I. Lebedev, S. Turner, A. Devi, R. A. Fischer and G. Van Tendeloo, *Int. J. Hydrogen Energy*, 2011, **36**, 15527-15537.
68 C. Sada, N. Argiolas, M. Bazzan and P. Mazzoldi, *Phys. Rev. B*, 2004, **69**, 144120.
69 J. Piella, F. Merkoci, A. Genc, J. Arbiol, N. G. Bastus and V. Puntes, *J. Mater. Chem. A*, 2017, **5**, 11917-11929.
70 H.-J. Kim and J.-H. Lee, *Sens. Actuators, B*, 2014, **192**, 607-627.